






## Magnetic super-structure and active surface role in the onset of magnetic excitons revealed in TbCu<sub>2</sub> nanoparticles

Elizabeth M. Jefremovas <sup>1,2</sup>✉, María de la Fuente Rodríguez <sup>1</sup>, Diego Alba Venero<sup>3</sup>,  
Cristina Echevarría-Bonet <sup>4</sup>, Philipp Bender<sup>1</sup>, Björn Fåk<sup>5</sup>, Jesús A. Blanco <sup>3</sup> & Luis Fernández Barquín <sup>1</sup>

Antiferromagnetic materials are receiving renewed interest on behalf of their potential for information technologies. Recent reports have also revealed how the physics governing such magnetic arrangements and their excitations become more complex compared to traditional ferromagnetic materials, especially at the nanoscale. Here, we address two main issues that are of prime interest to their technological transfer. First, using small-angle neutron scattering, we show the existence of a magnetic helix-like super-structure in a polycrystalline TbCu<sub>2</sub> alloy, preserved at both bulk and nanoparticle ensembles of 8 nm. Second, using inelastic neutron scattering, we elucidate the magnetic excitons and the crystalline electric field energy level schemes of TbCu<sub>2</sub> in bulk and nanoparticle ensembles. This allows to understand the effect of the surface broken symmetry on the quantum energy levels at the nanoscale, so as the key role of interfacial effects on the propagation of magnetic excitations. Our research provides insights for the realization of magnetic moment dynamics models based on complex nanometric super-structures, and for nanoparticles to be integrated in spintronics and information technology applications.

<sup>1</sup>Departamento CITIMAC, Facultad de Ciencias, Universidad de Cantabria, 39005 Santander, Spain. <sup>2</sup>Institute of Physics, Johannes Gutenberg University Mainz, 55099 Mainz, Germany. <sup>3</sup>ISIS Neutron and Muon Facility, Rutherford Appleton Laboratory, Didcot OX11 0QX, United Kingdom. <sup>4</sup>Department of Physics, University of Oviedo, 33007 Oviedo, Spain. <sup>5</sup>Institut Laue-Langevin, CS 20156, 38042 Grenoble Cedex 9 France. ✉email: [martinel@uni-mainz.de](mailto:martinel@uni-mainz.de)

The use and potentialities of antiferromagnetic (AF) materials has started a new era in the last decade. The 20<sup>th</sup> century paradigm, where AF materials were considered “interesting, but useless” (L. Néel<sup>1</sup>), has been completely changed in the second decade of the current 21st century. AFs display inherent assets, compared to the traditionally used ferromagnetic (FM) materials, that make them ideal candidates for the incoming spintronics-based technological devices<sup>2–4</sup>. AF structures are also a phenomenal playground for Fundamental Physics research, as the coupling among the magnetic moments can be settled in such a way that complex magnetic arrangements, beyond the simple idea of antiparallel arrangement, can flourish. These include helix, non-collinear and/or noncoplanar, to cite a few<sup>5–11</sup>, which are potential sources for topological spin textures to occur<sup>12–15</sup>.

Following this idea, in the last years, some of the already known AF structures are being revisited, aiming to look for these exotic magnetic phenomena and/or topologically-protected spin textures<sup>16,17</sup>. Nevertheless, up to our knowledge, there are no studies investigating whether these complex structures hold in nanoparticle ensembles or if the reduced dimensionality and/or symmetry breaking may destroy them. Moreover, the large number of interaction between the individual nanoparticles give rise to the so-called “super-magnetic” states<sup>18</sup> (Superparamagnetic, Superferromagnetic, Super Spin Glass etc.). These are extremely dependent on the inter-particle interactions and get modified in the presence of strong AF interactions. As an example, the mechanism for beating the Superparamagnetic limit has been reported for nanoparticle ensembles<sup>19,20</sup>. The question whether long-range correlations setting an AF magnetic super-structure may be affected in the nanoparticle regime is to be answered.

To complete the -understanding over AF materials, accessing and describing the energy level schemes and magnetic excitations would be demanded. Although inelastic neutron scattering (INS) technique is already standard in the case of single crystals<sup>21,22</sup>, the works concerning polycrystalline materials are less common<sup>23,24</sup>, being the ones depicting nanoparticles extremely scarce<sup>25</sup>, and nearly absent for 4f AFs<sup>26</sup>.

In this work, we have investigated the static and dynamic magnetic structure of TbCu<sub>2</sub> alloy, both in bulk and nanoparticle (8 nm) size. Previous works on TbCu<sub>2</sub><sup>27,28</sup> have shown that the bulk and magnetic nanoparticles (MNPs) keep essentially the same AF commensurate arrangement within the core<sup>27,29–31</sup>, while the surface magnetic moments give rise to a Spin Glass-like (SG) state<sup>27,28</sup>, resulting in a global Superantiferromagnetic (SAF) arrangement. Nevertheless, the question whether this alloy could host a more complex AF structure than that of a collinear-commensurate AF has remained unheard, to the best of our knowledge. To address this question, we have benefited from Small-Angle Neutron Scattering (SANS), a technique that allows the detection of magnetic super-structures that extend above the magnetic unit cell<sup>32</sup>. Concerning the access to the quantum energy levels, we have successfully conducted and analyzed inelastic neutron scattering (INS) measurements, thanks to which we have depicted the CEF levels of TbCu<sub>2</sub> bulk alloy, and monitoring how are they affected by the size reduction to the nanoscale. Although there has been a remarkable progress in understanding the evolution of magnetic ordered structures at the nanoscale<sup>25,33–35</sup>, the interplay between the size reduction and the magnetic interactions in ensembles of MNPs is still yet to be fully understood<sup>36</sup>. Indeed, the macroscopic properties of the different materials get altered by the size reduction to the nanoscale owing to a modification of the energy level schemes, which requires a remodeling of the CEF and collective excitations (magnons) along nanocrystallites and interfaces<sup>26,37–39</sup>. Here, we have moved one step beyond not only by describing the energy levels in bulk TbCu<sub>2</sub>, but also in nanoparticle ensembles. The

obtained results are not only essential to the basic understanding of magnetic materials at the nanoscale, yet they also provide sufficient evidence for MNPs to be considered as new-age potential candidates for spintronics and topological spin textures applications, or 2D interfacial effects, hot topic nowadays with the advent of new inspiring systems, to cite a few.

## Results and discussion

**Small-angle neutron scattering.** The magnetic structure of TbCu<sub>2</sub> has been described previously as a collinear commensurate AF with two propagation vectors  $\tau_\alpha = (0, 0, 0)$  and  $\tau_\beta = (1/3, 0, 0)$ , where the magnetic moments are aligned along the *a*-axis direction<sup>29,31</sup>. Depending upon their Miller index, two temperature dependencies for the magnetic moments are found: the ones indexed with odd Miller indexes (*h*, *k*, *l*) decrease faster upon increasing *T* compared to the ones indexed with even *h* + *k* + *l* and (*h* ± 1/3, *k*, *l*)<sup>30</sup>. This is also the case for TbCu<sub>2</sub> MNPs<sup>27,28</sup> and Tb<sub>0.5</sub>La<sub>0.5</sub>Cu<sub>2</sub>, both bulk and MNPs<sup>40</sup>, which underlines the robustness of such AF arrangement against size and/or magnetic dilutions. In the present work, we describe the finding of a magnetic super-structure in TbCu<sub>2</sub>, which could be described according to a spiral-like configuration. For that, Small-Angle Neutron Scattering (SANS) is the most suitable technique, as it allows to probe smaller momentum transfers, where additional (longer) magnetic correlations apart from the fundamental AF ones can be disclosed.

Figure 1 showcases the SANS patterns corresponding to bulk (top) and 8-nm-sized MNPs (bottom). 7-nm-sized MNPs have also been measured, allowing to further confirm the results obtained at 8 nm (see Supplementary Fig. 1 in Supplementary Note 1). Note the asymptotic power-law decay of the MNPs SANS intensity  $\propto q^{-4.3}$  in the low-*q* region, close to the typical  $I \propto q^{-4}$  corresponding to microstructures with sharp interfaces<sup>32,41</sup>. The form factor cannot be extracted from the measurements, owing to the powder state of the samples, the low signal stemming from such small nanoparticle sizes and indeed, to the size distribution of the nanoparticles, which further blurs any potential contribution from the nanoparticle form factor. Transmission electron micrographs (see Supplementary Fig. 2 in Supplementary note 2) showcase the quasi-spherical morphology of the nanoparticles. Analysis of the histogram point to a mean nanoparticle size of 7.4(1.6) nm.

On the other hand side, in the high-*q* region, all patterns in Fig. 1 showcase a clear Bragg peak, which emerges at  $q = 1.15(1) \text{ nm}^{-1}$  below 40 K ( $T < T_N$ ), for both bulk and MNPs. The *q* value of this peak corresponds to a lattice spacing of 54.6(1) Å, which is incommensurate with any of the (crystallographic) unit cell parameters. This reflection corresponds therefore to  $\tau_\alpha + 0.115 \text{ Å}^{-1}$ . Indeed, no satellite peaks can be distinguished for this incommensurate peak at such large *q* values. The magnetic-field dependence of the peak intensity (see Fig. 1a, c) perfectly follows the metamagnetic transitions along the *a*-axis reported for TbCu<sub>2</sub> single crystal<sup>42</sup>, which unambiguously reveals the magnetic nature behind this incommensurate structure. Furthermore, the insets of panels a and c depict the field evolution at  $T = 40 \text{ K}$  for both  $H_{\text{parallel}}$  and  $H_{\text{perp}}$  configurations, where it can be seen how the magnetic super-structure is more robust along the parallel than the perpendicular direction. For both configurations, the peak is destroyed for  $\mu_0 H \geq 2 \text{ T}$ , in perfect agreement with the aforementioned metamagnetic transitions<sup>42</sup>. We have obtained the magnetic moment carried by such super-structure, which is of  $\approx 14 \mu_B$  at  $T = 40 \text{ K}$ , which would lead to a projection on each crystallographic axis of 1.12, 1.77 and  $1.90 \mu_B/\text{Tb}$  at along *a*, *b* and *c* axis, respectively, never surpassing the  $97\text{D}2\mu_B/\text{Tb}^{3+}$  calculated for the free ion. These values would be compatible with an helix

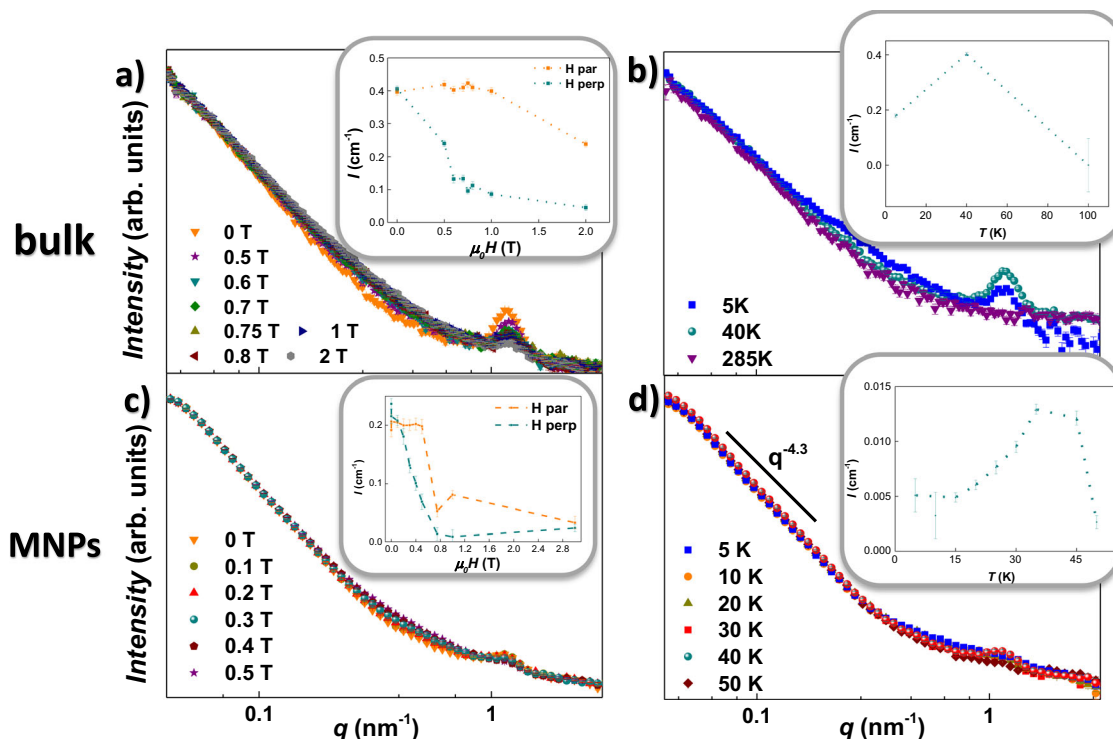


**Fig. 1 SANS intensity, measured in the perpendicular geometry, vs. momentum transfer  $q$  (log-log scale) corresponding to bulk and 8-nm-sized MNPs.** **a** and **c** display the patterns measured at  $T = 40$  K under several applied field between 0 and  $\mu_0 H = 2$  T; **b** and **d** include the patterns measured at temperatures between 5 and 285 K under no external applied field. The insets display the intensity evolution of the peak found at  $1.15 \text{ nm}^{-1}$  with the applied field and with temperature.

configuration laying in  $bc$ -plane. We propose an helix to be the most reasonable configuration of the magnetic moments, as pure Tb, Dy, and Ho display such structure<sup>43,44</sup>, so as it does metallic nanocrystalline Tb<sup>45</sup>, which also presents a peak located at the same  $q \approx 1.15 \text{ nm}^{-1}$  value. By assuming such a configuration, by analogy to the case of metallic terbium<sup>43</sup>, the new incommensurate propagation vector would be  $\tau \sim 1/12$  in reduced wave vector units. The turn angle or pitch of the helical component will be around 30 degrees. Besides the projection of the magnetic moment along crystallographic each axis, the stabilization of the helical configuration in our system is also supported by the strong contribution of the magnetic anisotropy energy, described classically by the six-order crystalline electric field parameters (see INS results and Supplementary Section).

Cooling down to 5 K (see Fig. 1b), the intensity of the peak diminishes (see insets in b and d panels), which is well accounted by the decrease of the ratio  $\tau_\beta/\tau_\alpha$  ( $\tau_\beta = (1/3, 0, 0)$  and  $\tau_\alpha = (0, 0, 0)$ , propagation vectors) between  $T = 42$  K to  $T = 23.5$  K<sup>30</sup>. No trace for this peak is observed in the paramagnetic (PM) region, ensuring that it must be ascribed to the AF state of the alloy.

It is specially remarkable the robustness of such super-structure against size reduction, as it can be observed in Fig. 1b, d. Even if partially masked by the increased spin-misalignment contribution induced by the surface disorder<sup>46,47</sup>, the incommensurate peak in the MNPs is clearly visible. Indeed, the correlations among the magnetic moments forming the super-structure are affected by the increasing disorder, as the peak gets broader, less robust against the applied magnetic field (remaining only for  $\mu_0 H \leq 0.5$  T) and slightly shifts towards lower  $q$  values (from  $1.15(1)$  to  $1.13(1) \text{ nm}^{-1}$ ). Nevertheless, the structure retains the same prevalence than the bulk to be robust in the  $H_{par}$  compared to the  $H_{perp}$ .

The prevalence of the magnetic super-structure in these TbCu<sub>2</sub> MNPs is very remarkable, as other RCu<sub>2</sub> ensembles have

evidenced a clear tendency towards disorder (SG) arising from the competition between frustration and ordered states<sup>35,40,48</sup>. The frustration ascribed to the surface SG-phase of TbCu<sub>2</sub> MNPs (see Supplementary Note 3, time-dependent phenomena, and Supplementary Fig. 3) is weaker compared to that of other RCu<sub>2</sub> MNP ensembles, together with a strong anisotropy, which may account for the prevalence of such super-structure.

**Inelastic neutron scattering.** Tb<sup>3+</sup> is a non-Kramers ion with a total angular momentum  $J = 6$ . A CEF with  $C_{2v}$  symmetry splits the degeneracy of  $J$  in  $2J + 1 = 13$  singlets. In order to describe the CEF energy level schemes of TbCu<sub>2</sub>, it is easier to analyze the INS spectra of the diluted alloy, Tb<sub>0.1</sub>Y<sub>0.9</sub>Cu<sub>2</sub>, which does not order magnetically<sup>40,49</sup>. These CEF schemes hold in the paramagnetic (PM) region of TbCu<sub>2</sub> (i.e.,  $T > T_N = 48$  K), and also below  $T_N$  by including the molecular field, which shifts the energy levels, and also splits them (Zeeman effect). Indeed, magnetic excitations may also happen below the ordering temperature. Therefore, we will begin by analyzing non-magnetic bulk Tb<sub>0.1</sub>Y<sub>0.9</sub>Cu<sub>2</sub>, and afterwards, we will unravel the schemes in TbCu<sub>2</sub> bulk and 7-nm-sized nanoparticles.

The INS spectra of Tb<sub>0.1</sub>Y<sub>0.9</sub>Cu<sub>2</sub> measured at  $3.06 \text{ \AA}$  ( $E_0 = 8.74$  meV) and  $T$  range from 1.5 to 100 K are included in Fig. 2a. We have also measured the INS at incoming neutron wavelength of 2.2 and 1.1  $\text{ \AA}$  (16.9 and 67.7 meV, respectively), yet no remarkable findings are observed. Two clear magnetic excitations, located at  $E = 5.3$  and  $6.1 (\pm 0.1)$  meV, can be seen. From 20 K, two additional excitations appear at 3.5 and close to 4.3 meV, corresponding to transitions from thermally excited levels. The energies of the crystal field levels are essentially  $T$ -independent, at least up to  $T = 40$  K, and soften only slightly at  $T = 100$  K. The width in energy of the crystal-field peaks are resolution limited up

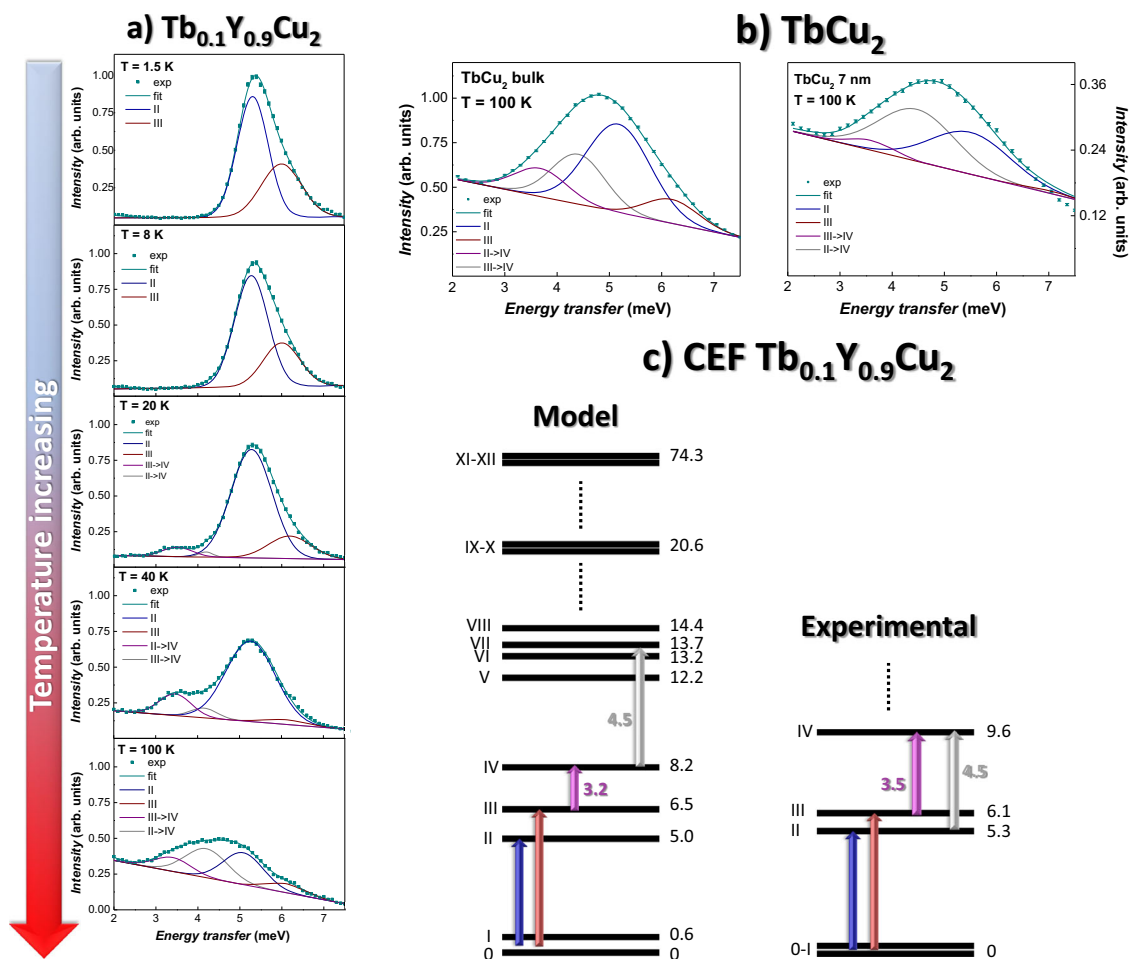


**Fig. 2** Inelastic neutron scattering spectra for crystalline electric field energy level schemes determination. **a** Includes the spectra for  $\text{Tb}_{0.1}\text{Y}_{0.9}\text{Cu}_2$  bulk alloy measured at several temperatures between  $T = 1.5$ – $100$  K (top to bottom) at incident neutron energy  $E_0 = 8.74$  meV and  $Q = 1.75 \text{ \AA}^{-1}$ . The intensities have been normalized to 5.3 meV excitation. **b** Showcases the INS spectra corresponding to  $\text{TbCu}_2$  (bulk, left and 7 nm MNPs, right) at  $T = 100$  K (paramagnetic region), measured at  $E_0 = 16.9$  meV and  $Q = 1.75 \text{ \AA}^{-1}$ . **c** Includes the energy level schemes corresponding to the CEF splitting of  $\text{Tb}^{3+}$  ion under  $C_{2v}$  symmetry in the absence of molecular field. A comparison between the calculated (model) and the experimentally observed levels is provided. Note the colors of the arrows marking the transitions match the peaks observed in **a** and **b**. Details on the calculations are provided in the Supplementary Notes 4 and 5.

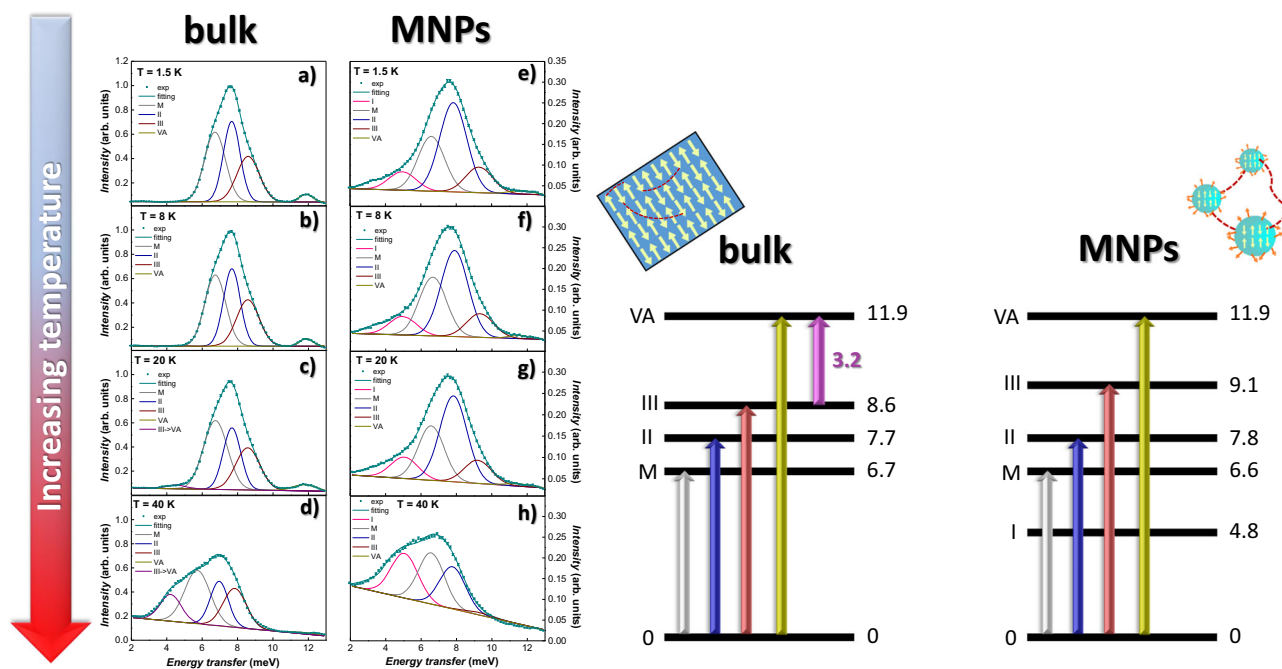
to  $T = 20$  K, while for higher temperatures a small intrinsic energy width is observed.

Figure 2c includes a comparison between a calculated crystal-field model and our experimental findings. The model has been calculated using the program Searchspace and Sumanfit in the McPhase package<sup>50</sup>, with crystal-field parameters from Andreev et al.<sup>51</sup> as starting values. Simulated annealing was then performed using the program Simann in McPhase. A more detailed explanation over the calculations is provided in Supplementary Notes 4 and 5. The detailed compositions of the crystalline electric field states are included in Supplementary Table 1. According to Fig. 2c, it is easy to see how our experimental results are in good agreement with the model. The calculation also predicts additional thermally induced transition at even lower energies, but they are hidden by the strong elastic peak. On the other hand side, transitions at energy values above 12 meV are also predicted by our model. Nevertheless, these are almost impossible to probe experimentally considering the instrumental resolution, since their intensity is too low. The evaluation of the INS spectra at 67.6 meV (see Supplementary Figs. 5 and 6 in Supplementary Note 6) provides some hints of two humps at around 12–15 and 25 meV. While the later are

account for phonon scattering, since the intensity of this excitation increases with the wave vector transfer  $q$ , the former could stem from the convolution of energy levels V–VIII in our proposed model presented in Fig. 2c. Notwithstanding, the intensity of this peak is at the resolution limit, thus, we would rather guarantee the validity of our model until 10 meV (IV excitation). Comparing with the literature, our results are also in good agreement with the ones reported for bulk  $\text{TbCu}_2$  alloy by Rotter et al.<sup>23</sup>.

The INS spectra of  $\text{TbCu}_2$  in the paramagnetic (PM) range, shown in Fig. 2b at  $T = 100$  K, are very alike to those of  $\text{Tb}_{0.1}\text{Y}_{0.9}\text{Cu}_2$ , as expected. Comparing bulk and MNP ensembles, we can observe that the energy levels are slightly shifted downwards (around  $-0.5$  meV) for the latter, a feature that agrees with the softening of CEF levels reported for systems with interfaces and grain boundaries<sup>26,38</sup>.

Figure 3 includes the temperature dependence of the INS spectra within the magnetically-ordered region ( $T < T_N$ ) for bulk and 7-nm-sized MNPs measured at incoming neutrons of  $2.2 \text{ \AA}$  ( $E_0 = 16.9$  meV), since only the excitations below 12 meV display such an intensity to be considered as real excitations by the instrumental resolution being. As the temperature is lowered



**Fig. 3** Inelastic neutron scattering spectra vs. energy transfer measured at  $E_0 = 17$  meV and  $Q = 1.75 \text{ \AA}^{-1}$  for the magnetic  $\text{TbCu}_2$  alloys. **a–d** include the spectra for bulk, and **e–h**, the ones for 7-nm-sized MNPs, measured at several  $T$  between 1.5 and 40 K. The INS intensity has been normalized to the bulk III intensity. The sketch on the right side displays the energy level schemes of  $\text{TbCu}_2$  (bulk and MNPs) in the magnetic region, where the splitting is affected by both CEF and RKKY effects. This scheme is in good agreement with calculations performed by Andreucut et al.<sup>57</sup>. A shift of 2 meV arising from the molecular field can be easily observed compared to the sketch shown in Fig. 2.

below  $T_N$ , the scattering is completely dominated by the 5 meV level (pushed up to about 7 meV at low temperature by means of the molecular field), which becomes dispersive due to exchange interactions (note the slightly structured non-Gaussian profile of the excitation). This 2 meV shift of the energy levels is well accounted by a molecular field of magnitude  $\approx 60$  T, calculated according to the low-temperature equal-moment magnetic structure of  $\text{TbCu}_2$ , which yields to an equal-exchange (equal-molecular field) of the same magnitude on all the magnetic ions  $\text{Tb}^{3+}$  (as demonstrated in the calculations discussed in Supplementary Notes 4 and 5). Needless to say, the validity of this calculation is secured thanks to the validation using the low-temperature data ( $T = 1.5$  K), where the thermal excitations are minimized and the equal-moment structure (see SANS results) holds. Besides causing a positive shift of the energy transfer, the molecular field may also split the energy levels (Zeeman splitting) up to  $\approx 5$  meV for the case of  $T_N \approx 50$  K. Therefore, the peak found at 11.9(1) meV in Fig. 3 (labeled as “VA”) may be ascribed to the splitting of a ground state level above the experimental energy windows (see Fig. 2a and model in c). At 6.7(1) meV, a transition (labeled as “M”), which was not observed in the paramagnetic region (See Fig. 2b), is found. In contrast to the VA excitation, the intensity of the M-one reduces as the temperature is increased, following the behavior of a magnetic excitation<sup>52</sup>. Finally, upon increasing the temperature, thermally activated transitions from excited levels occur, as it was the case of  $\text{Tb}_{0.1}\text{Y}_{0.9}\text{Cu}_2$ . Note the temperature dependence of the peak labeled as III  $\rightarrow$  IV. So does the peak labeled as IIA, which increases in intensity with  $T$ , indicating that this excitation also corresponds to the energy between two excited levels.

The energy transfer values of the peaks in the MNPs, displayed in Fig. 3e–h, are in good agreement with those corresponding to the bulk alloy. As a brief reminder, nanoparticles should behave differently from bulk ensembles owing to their surface symmetry breaking, reduced coordination and dimensionality. These

features modify the interactions among the magnetic moments, which obviously include the magnetic ones. Actually, it is the lack of energy shift which provides powerful information about the modifications of the RKKY excitations undergone at the nanoscale. For a splitting purely driven by CEF effects, a negative shift of the peaks for the nanoparticle ensembles must be observed, owing to microstrain and disorder<sup>26,38</sup>. This was the case of  $\text{TbCu}_2$  MNPs in the PM region (see Fig. 2b), so was the case of  $\text{NdCu}_2$  NPs<sup>26</sup>. Nevertheless, this does not hold for  $\text{TbCu}_2$  nanoparticles below  $T_N$ . The lack of energy shift reveals that there must exist a contribution in the nanoparticles causing the positive energy shift of the energy levels, which is of similar magnitude to the CEF splitting. Therefore, we propose that, additional to the bulk molecular field of 60 T, that is preserved at the core magnetic moments<sup>35</sup>, an additional surface molecular field must be realized at the nanoparticles. This would be appear necessarily as a consequence of the reduced dimensionality, coordination, symmetry breaking and anisotropy. Hence, the surface moments will trigger the onset of magnetic excitons at 6.7(1) meV. The existence of an active surface in the RKKY propagation has already been reported in  $\text{NdCu}_2$  MNPs<sup>26</sup>, where the presence of magnons was reported. As corresponds to magnetic excitations, this contribution decreases as the Néel transition is approached. Already in the vicinity of the Néel transition, a negative displacement of about  $-0.4$  meV is observed, which is well accounted for a pure CEF softening, revealing the disappearance of such additional contribution. For  $T \gg T_N$ , a purely CEF-driven softening of  $-0.4(1)$  meV is kept constant, backing up our finding.

Coming now to the peak intensity, which reveals the probability of transitions between energy levels, all the peaks are reduced in intensity and broaden in the MNPs, compared to the bulk. This general trend is expected owing to the increased disorder in the nanoparticle ensembles. Here, the most striking finding is the partial inhibition of transitions to M and III,

accounted by the reduction of the peak area  $Intensity \cdot FWHM$  relative to transitions to II ( $r = Area_I/Area_{II}$  for  $i = M$  and  $i = III$ ). Notice how, for the bulk alloy, the peak area for M and II was roughly the same ( $r = 0.96$ ), while III was  $r = 0.7$ . In the case of the MNPs, the relative area of M is drastically reduced to almost half ( $r = 0.6$ ), so does the one of III ( $r = 0.3$ ). This partial inhibition indicates a significant modification of the dipolar transitions from the ground state to levels IIA and III, which in turn points to a reduction in the value of the matrix elements that determine the transition probabilities. Such a change shall be caused by a significant alteration in the way magnetic interactions are propagated in bulk and nanostructured samples, which can be understood by the surface-driven modifications of the RKKY exchanged interactions, caused to the local-symmetry modifications and interfaces at the nanoparticles. Furthermore, the modification of the RKKY exchanged interaction has already been reported in  $NdCu_2$  MNPs<sup>26</sup>. The modification of the matrix elements can also be accounted by the appearance of an excitation at 4.8(1) meV (marked as “I” in Fig. 3). This excitation is due to the splitting of the ground state, which, according to the model shown in Fig. 2c), can be considered a quasideublet. This quasideublet is split due to the RKKY interactions, enabling a transition which could be found even up to 5 meV. From our experimental data in  $TbCu_2$  bulk alloy, this transition is not visible, but for the MNPs, the reduced dimensionality alters the matrix elements in such a way that the probability of transitions to this state increases, making this excitation clearly observed. Finally, the peak labeled as “VA” also accounts for the modification of matrix elements, since its intensity is poorly defined compared to the bulk situation.

Indeed, one could not discard the presence of energy levels above 12 meV for  $TbCu_2$ , also pointed by Rotter et al.<sup>23</sup>. As we have already discussed for  $Tb_{0.1}Y_{0.9}Cu_2$ , our model leads to a very large splitting, around 70 meV, yet their corresponding transition matrix elements are very small. Our experimental results at 67 meV (see Supplementary Note S6) provide some hints of transitions at 12–15 and 25 meV, although their intensity is too low to meet our accuracy criteria for being included in the discussions. We have performed specific heat measurements (see Supplementary Fig. 7 in Supplementary Note 7) to access more information on about the large splitting. The magnetic entropy at 300 K,  $S_{exp}(300K) = 10 \text{ J/K}^2\text{mol}$ , is well below the theoretical  $S_{theo} = R \cdot \ln(2J + 1) = 21.3 \text{ J/K}^2\text{mol}$ , which implies that the CEF total splitting is not accomplished at RT. Briefly, this means there should be more CEF levels at higher energy values.

## Conclusion

In this work, we have reported the observation of a magnetic super-structure in polycrystalline  $TbCu_2$ , which shall be conformed following an helix-like configuration. The new incommensurate propagation vector would be  $\tau \sim 1/12$  in reduced wave vector units, and the turn angle or pitch of the helical component will be around 30 degrees. This incommensurate structure is robust against size reduction, as it holds in nanoparticle sizes of 8 nm. The existence of this newly reported incommensurate magnetic structure could be used to revisit the Hamiltonian terms used in Rare Earth intermetallic alloys, which would constitute an ideal playground to find potential magnetic super-structures, but also paves the way for the experimental realization of magnetic super-structures in crystalline nanoparticle ensembles below 10 nm with a relatively simple top-down production route.

Moreover, we have been able to describe the energy level diagram of  $TbCu_2$  in both bulk and nanoparticle ensembles. We have provided a model which accounts very well for the CEF splitting and the magnetic excitons. Furthermore, it has been

shown how the symmetry breaking caused by the nanoparticle surface adds a term to the Hamiltonian of the system, modifying both single-ion (CEF) and magnetic (RKKY-driven) excitations. This finding highlights the different role of the core and surface environments at the CEF and magnon propagation, endorsing the dual-spin dynamics (core and surface) of magnetic nanoparticles. A step forward for this research would be focused on determining whether the observed magnetic excitons could already be defined as magnons. For this, the definition of the energy levels and energy dispersion curves must be improved, which shall be possible in the future using eventual single crystals and polarized inelastic neutron scattering.

The results discussed in this work showcase the robustness of incommensurate magnetic structures, which is of primer interest for spintronic applications, plus improves the understanding on how the interplay between the size reduction and the magnetic interactions in ensembles of magnetic nanoparticles occur, as it has been shown how the surface symmetry breaking influences the magnetic dynamics. The functional role of surface geometry has been demonstrated very recently theoretically and numerically for the initiation of pattern propagation by Nishide and Ishihara<sup>53</sup>, following the thread of several up-to-date works also demonstrating the functional role of the topology and geometry of surfaces in pattern formation<sup>54,55</sup>. So far to us, the present work constitutes one of the few case examples which shows and describes these claims experimentally in nanoparticle ensembles. The community of researchers working in complex magnetic materials requires still more (similar) combined SANS and INS evidences coming from other types of compounds within the nanoscale range to broaden a new field and to ponder to achieving an improved insight.

## Methods

**Sample fabrication.** Polycrystalline pellets of  $TbCu_2$  have been produced using an arc furnace (MAM-1, Johanna Otto GmbH) under an Ar atmosphere (99.99%). The alloys were sealed-off under Ar atmosphere (99.99%) and nanoscaled via ball milling (high-energy planetary Retsch PM 400/2). We have selected milling times  $t = 2$  and 5 h, as our previous experience indicates these  $t$  to be enough to achieve nanoparticle sizes  $\langle D \rangle$  of 8(1) nm and 7(1) nm, respectively<sup>28</sup>. We would like to emphasize that it is the use of this grinding technique which allows to produce the sufficient amount of MNPs (~12 g MNPs) required for INS measurements.

**Small-angle neutron scattering.** Small-angle neutron scattering (SANS) measurements have been carried out at the SANS2D time-of-flight instrument (ISIS, UK) using a wavelength range between  $1.75 \text{ \AA} < \lambda < 16.5 \text{ \AA}$ , sample temperatures between 5–285 K, and applied fields  $\mu_0 H$  between 0–6 T. A measuring time of 0.5 h for each scattering pattern was chosen to assure a high signal-to-noise ratio. Experiment <https://doi.org/10.5286/ISIS.E.RB1910077>.

**Inelastic neutron scattering.** Inelastic neutron scattering measurements were performed on  $Tb_{0.1}Y_{0.9}Cu_2$  and  $TbCu_2$  using IN4 neutron time-of-flight spectrometer at the ILL (France), using incident neutron energies of  $E_0 = 8.74, 16.7$  and  $67.6 \text{ meV}$ , and  $Q = 1.75 \text{ \AA}^{-1}$ . INS measurements at IN6 (see Supplementary Note S6) were measured with  $E_0 = 3.1 \text{ meV}$ . The temperature was varied between 1.5 and 100 K to explore the different magnetic states of the alloys. All spectra were corrected for background, absorption, and self-shielding, and normalized to vanadium.

**Heat capacity measurements.** Heat capacity measurements were performed on compacted disks (~5 mg) following the relaxation method<sup>56</sup> under no external applied field within the temperature range of 2–300 K.

**Transmission electron microscopy.** TEM images were collected in a Jeol 2100 instrument at 200 kV of milled (powdered) samples deposited onto a conventional grid.

## Data availability

All data generated or analyzed during this study are included in this published article and its supplementary information files.

Received: 13 February 2023; Accepted: 26 July 2023;

Published online: 04 August 2023

## References

- Néel, L. Magnetism and local molecular field. *Science* **174**, 985–992 (1971).
- Jungwirth, T., Marti, X., Wadley, P. & Wunderlich, J. Antiferromagnetic spintronics. *Nat. Nanotechnol.* **11**, 231–241 (2016).
- Baltz, V. et al. Antiferromagnetic spintronics. *Revs. Modern Phys.* **90**, 015005 (2018).
- Jungfleisch, M. B., Zhang, W. & Hoffmann, A. Perspectives of antiferromagnetic spintronics. *Phys. Lett. A* **382**, 865–871 (2018).
- Binz, B., Vishwanath, A. & Aji, V. Theory of the helical spin crystal: a candidate for the partially ordered state of MnSi. *Phys. Rev. Lett.* **96**, 207202 (2006).
- Tewari, S., Belitz, D. & Kirkpatrick, T. Blue quantum fog: chiral condensation in quantum helimagnets. *Phys. Rev. Lett.* **96**, 047207 (2006).
- Pathak, S. A. & Hertel, R. Three-dimensional chiral magnetization structures in FeGe nanospheres. *Phys. Rev. B* **103**, 104414 (2021).
- Lalena, V., Bustingorry, S. & Campo, J. Dynamics of chiral solitons driven by polarized currents in monoaxial helimagnets. *Sci. Rep.* **10**, 1–10 (2020).
- Feng, W. et al. Topological magneto-optical effects and their quantization in noncoplanar antiferromagnets. *Nat. Comm.* **11**, 1–9 (2020).
- Boventer, I. et al. Room-temperature antiferromagnetic resonance and inverse spin-Hall voltage in canted antiferromagnets. *Phys. Rev. Lett.* **126**, 187201 (2021).
- Elmers, H.-J. et al. Néel vector induced manipulation of valence states in the collinear antiferromagnet Mn<sub>2</sub>Au. *ACS Nano* **14**, 17554–17564 (2020).
- Yu, X. et al. Transformation between meron and skyrmion topological spin textures in a chiral magnet. *Nature* **564**, 95–98 (2018).
- Dong, B.-W. et al. Spin hall magnetoresistance in the non-collinear ferrimagnet GdIG close to the compensation temperature. *J. Phys. Cond. Matt.* **30**, 035802 (2017).
- Prychynenko, D. et al. Magnetic skyrmion as a nonlinear resistive element: a potential building block for reservoir computing. *Phys. Rev. Appl.* **9**, 014034 (2018).
- Jaiswal, S. et al. Investigation of the dzyaloshinskii-moriya interaction and room temperature skyrmions in W/CoFeB/MgO thin films and microwires. *Appl. Phys. Lett.* **111**, 022409 (2017).
- Karna, S. K. et al. Helical magnetic order and Fermi surface nesting in noncentrosymmetric ScFeGe. *Phys. Rev. B* **103**, 014443 (2021).
- Wilde, J. M. et al. Helical magnetic ordering in Sr (Co<sub>1-x</sub>Ni<sub>x</sub>)<sub>2</sub>As<sub>2</sub>. *Phys. Rev. B* **100**, 161113 (2019).
- Bedanta, S. & Kleemann, W. Supermagnetism. *J. Phys. D Appl. Phys.* **42**, 013001 (2008).
- Skumryev, V. et al. Beating the superparamagnetic limit with exchange bias. *Nature* **423**, 850–853 (2003).
- Nogués, J. et al. Exchange bias in nanostructures. *Phys. Rep.* **422**, 65–117 (2005).
- Lawrence, J., Shapiro, S., Sarrao, J. & Fisk, Z. Inelastic neutron scattering in single-crystal YbInCu<sub>4</sub>. *Phys. Rev. B* **55**, 14467 (1997).
- Mittal, R. et al. Measurement of anomalous phonon dispersion of CaFe<sub>2</sub>As<sub>2</sub> single crystals using inelastic neutron scattering. *Phys. Rev. Lett.* **102**, 217001 (2009).
- Rotter, M. et al. Pressure dependence of the magnetic structures and excitations in the giant magnetostriction compound TbCu<sub>2</sub>. *J. Mag. Mag. Mat* **269**, 372–379 (2004).
- Gratz, E. et al. Structural, magnetic, electronic and transport properties of NdCu<sub>2</sub>. *J. Phys. Cond. Matt.* **3**, 9297 (1991).
- Mørup, S., Madsen, D. E., Frandsen, C., Bahl, C. R. & Hansen, M. F. Experimental and theoretical studies of nanoparticles of antiferromagnetic materials. *J. Phys. Cond. Matt.* **19**, 213202 (2007).
- Jefremovas, E. M. et al. Observation of surface magnons and crystalline electric field shifts in superantiferromagnetic NdCu<sub>2</sub> nanoparticles. *Phys. Rev. B* **104**, 134404 (2021).
- Echevarria-Bonet, C. et al. Size-induced superantiferromagnetism with reentrant spin-glass behavior in metallic nanoparticles of TbCu<sub>2</sub>. *Phys. Rev. B* **87**, 180407(R) (2013).
- Echevarria-Bonet, C. et al. Magnetic phase diagram of superantiferromagnetic TbCu<sub>2</sub> nanoparticles. *J. Phys. Cond. Matt.* **27**, 496002 (2015).
- Lebech, B., Smetana, Z. & Sima, V. Magnetic structures and related properties of some rare-earth intermetallic compounds, RCu<sub>2</sub>. *J. Mag. Mag. Mat* **70**, 97–101 (1987).
- Sima, V., Smetana, Z., Lebech, B. & Gratz, E. Temperature dependence of the magnetic structure of TbCu<sub>2</sub>. *J. Mag. Mag. Mat* **54**, 1357–1358 (1986).
- Luong, N. H. & Franse, J. Magnetic properties of rare earth–Cu<sub>2</sub> compounds. *Handb. Magn. Mater.* **8**, 415–492 (1995).
- Michels, A. *Magnetic Small-Angle Neutron Scattering: A Probe for Mesoscale Magnetism Analysis*, vol. 16 (Oxford University Press, 2021).
- Purwins, H.-G., Houmann, J., Bak, P. & Walker, E. Interaction between magnons and magnetic excitons in TbAl<sub>2</sub>. *Phys. Rev. Lett.* **31**, 1585 (1973).
- Tronc, E. Magnetic relaxation in fine-particle systems. *Adv. Chem. Phys.* **283**, 283–449 (1997).
- Jefremovas, E. et al. Magnetic order and disorder environments in superantiferromagnetic NdCu<sub>2</sub> nanoparticles. *Sci. Rep.* **12**, 1–10 (2022).
- Peddis, D., Laureti, S. & Fiorani, D. *New Trends in Nanoparticle Magnetism* (Springer, 2021).
- Golosovsky, I. et al. Magnetic excitations and exchange interactions in the substituted multiferroics (Nd, Tb) Fe<sub>3</sub>(BO<sub>3</sub>)<sub>4</sub> revealed by inelastic neutron scattering. *Phys. Rev. B* **103**, 214412 (2021).
- Baczewski, L., Piecuch, M., Durand, J., Marchal, G. & Delcroix, P. Influence of interface effects on a rare-earth crystal field in iron–rare-earth multilayers. *Phys. Rev. B* **40**, 11237 (1989).
- Zhao, L. et al. Influences of element segregation on the magnetic properties in nanocrystalline Nd-Ce-Fe-B alloys. *Mater. Charact.* **148**, 208–213 (2019).
- Jefremovas, E. M. et al. Exploring the different degrees of magnetic disorder in Tb<sub>x</sub>R<sub>1-x</sub>Cu<sub>2</sub> nanoparticle alloys. *Nanomaterials* **10**, 2148 (2020).
- Hammouda, B. A new Guinier–Porod model. *J. Appl. Crystallogr.* **43**, 716–719 (2010).
- Hashimoto, Y., Fujii, H., Fujiwara, H. & Okamoto, T. Magnetic properties of rare earth copper intermetallic compounds, RCu<sub>2</sub>, I. heavy rare earth. *J. Phys. Soc. Jpn* **47**, 67–72 (1979).
- Jensen, J. & Mackintosh, A. R. *Rare Earth Magnetism* (Clarendon Press Oxford, 1991).
- Chatterji, T. *Neutron Scattering from Magnetic Materials* (Elsevier, 2005).
- Michels, A. et al. Influence of crystallite size and temperature on the antiferromagnetic helices of terbium and holmium metal. *Phys. Rev. B* **83**, 224415 (2011).
- Weissmüller, J. et al. Spin structure of nanocrystalline terbium. *Phys. Rev. B* **69**, 054402 (2004).
- Bersweiler, M. et al. Unraveling the magnetic softness in Fe–Ni–B-based nanocrystalline material by magnetic small-angle neutron scattering. *IUCrJ* **9**, 65–72 (2022).
- M Jefremovas, E., Svedlindh, P. & Fernández Barquín, L. Dual magnetic disorder dynamics in orbital free moment GdCu<sub>2</sub> superantiferromagnetic nanoparticles. *J. Nanoparticle Res.* **24**, 194 (2022).
- Hien, T. et al. Magnetic properties of rCu<sub>2</sub> (r = dy, ho, er) and Dy<sub>x</sub>Y<sub>1-x</sub>Cu<sub>2</sub> compounds. *J. Mag. Mag. Mat* **31**, 245–246 (1983).
- Rotter, M., Le, M. D., Boothroyd, A. T. & Blanco, J. A. Dynamical matrix diagonalization for the calculation of dispersive excitations. *J. Phys.: Condens. Matt.* **24**, 213201 (2012).
- Andreev, A., Bartashevich, M., Goto, T., Diviš, M. & Svoboda, P. High-field transition in TbCu<sub>2</sub>. *Phys. B Cond. Matt.* **246**, 479–482 (1998).
- Boothroyd, A. T. *Principles of Neutron Scattering from Condensed Matter* (Oxford University Press, 2020).
- Nishide, R. & Ishihara, S. Pattern propagation driven by surface curvature. *Phys. Rev. Lett.* **128**, 224101 (2022).
- Horibe, K., Hironaka, K.-i, Matsushita, K. & Fujimoto, K. Curved surface geometry-induced topological change of an excitable planar wavefront. *Chaos* **29**, 093120 (2019).
- Ai, B.-Q., Zhu, W.-J. & Liao, J.-J. Collective transport of polar active particles on the surface of a corrugated tube. *N. J. Phys.* **21**, 093041 (2019).
- Bachmann, R. et al. Heat capacity measurements on small samples at low temperatures. *Rev. Sci. Instr.* **43**, 205–214 (1972).
- Andrecut, M., Pop, I. & Burda, I. Calculation of the crystal field and paramagnetic susceptibility of intermetallic compounds (Tb<sub>x</sub>Y<sub>1-x</sub>)Cu<sub>2</sub> and Tb(Cu<sub>x</sub>Ni<sub>1-x</sub>)<sub>2</sub>. *J. Phys. D Appl. Phys.* **26**, 1144 (1993).

## Acknowledgements

This work has been financially supported by Spain's MCIU MAT2017–83631–C3–R, MAGNES SV–PA–21–AYD/2021/51822 and PID2022–138256NB–C21 projects. Dr. L. Rodríguez Fernández and the SERMET service of the University of Cantabria are acknowledged for the TEM images E.M.J. acknowledges the Alexander von Humboldt Foundation for the “Alexander von Humboldt Postdoctoral Fellowship”. We acknowledge the ISIS Neutron and Muon Facility (DOI: 10.5286/ISIS.ERB1910077) and Institut Laue–Langevin (Proposal Ref. 4–04–486, 4–04–493 and 4–05–6265) for allocation of beamtime and resources.

## Author contributions

E.M.J., J.A.B. and L.F.B. wrote the paper. D.A.V. performed the SANS data reduction. M.F. and B.F. performed the INS data reduction. E.M.J., J.A.B., D.A.V. and P.B. analyzed the data. D.A.V., M.F., C.E.B. and L.F.B. set up and carried out the SANS experiment. B.F., J.A.B., M.F. and L.F.B. set up and carried out the INS experiment. E.M.J. and M.F. prepared and characterized the TbCu<sub>2</sub> samples. J.A.B. and L.F.B. coordinated the project. All authors discussed the results and contributed to the writing of the manuscript.

**Funding**

Open Access funding enabled and organized by Projekt DEAL.

**Competing interests**

The authors declare no competing interests.

**Additional information**

**Supplementary information** The online version contains supplementary material available at <https://doi.org/10.1038/s43246-023-00384-1>.

**Correspondence** and requests for materials should be addressed to Elizabeth M. Jefremovas.

**Peer review information** *Communications Materials* thanks the anonymous reviewers for their contribution to the peer review of this work. Primary Handling Editor: Aldo Isidori.

**Reprints and permission information** is available at <http://www.nature.com/reprints>

**Publisher's note** Springer Nature remains neutral with regard to jurisdictional claims in published maps and institutional affiliations.



**Open Access** This article is licensed under a Creative Commons Attribution 4.0 International License, which permits use, sharing, adaptation, distribution and reproduction in any medium or format, as long as you give appropriate credit to the original author(s) and the source, provide a link to the Creative Commons licence, and indicate if changes were made. The images or other third party material in this article are included in the article's Creative Commons licence, unless indicated otherwise in a credit line to the material. If material is not included in the article's Creative Commons licence and your intended use is not permitted by statutory regulation or exceeds the permitted use, you will need to obtain permission directly from the copyright holder. To view a copy of this licence, visit <http://creativecommons.org/licenses/by/4.0/>.

© The Author(s) 2023